High resolution three dimensional partially coherent diffraction imaging: Supplementary Information.

J. N. Clark[1,*], X. Huang[1], R. Harder[2] & I. K. Robinson[1,3]

[1]*London Centre for Nanotechnology, University College, London WC1E 6BT, UK*

[2]*Advanced Photon Source, Argonne, IL 60439, USA*

[3]*Research Complex at Harwell, Didcot, Oxfordshire OX11 0DE, UK*

Supplementary Figures

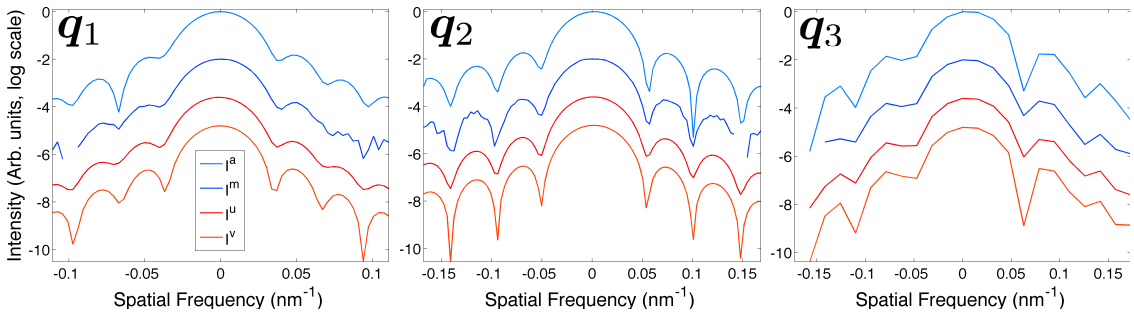

Supplementary Figure S 1: **Comparison of the reconstructed intensity with the measured data.** Lineouts from the detector x direction (left). Shown is the estimate of the measured intensity assuming full coherence, I^a which is compared to the measured intensity, I^m, the estimate of the measured intensity, I^u, from the partially coherent reconstruction and the coherent intensity, I^v, from the partially coherent reconstruction. Also shown are lineouts for the detector y (center) and scan direction (right).

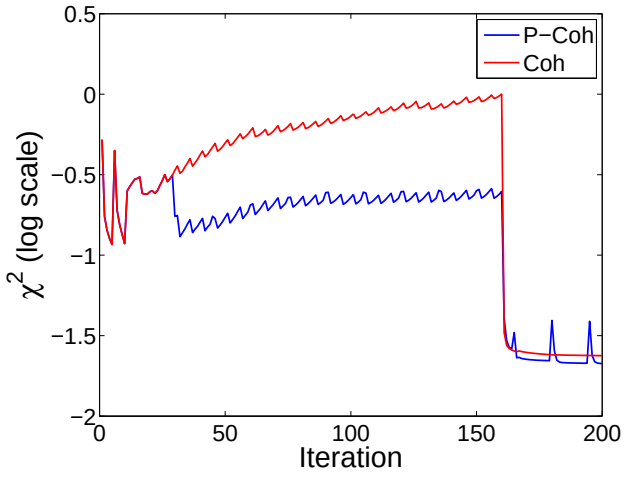

Supplementary Figure S 2: **Plot of the error metric as a function of iteration number.** Shown is the error metric for the reconstruction assuming full coherence (Coh, red line) compared to the partially coherent reconstruction (P-Coh, blue line). The error metric is for the reconstruction using the low coherence data set shown in the main text.

Supplementary Methods

The data were collected using a charged coupled device with pixel size of 20 μm. To increase the signal to noise ratio a binning of 2x2 was applied in the detector x and y directions. The binning was applied after a background image was subtracted and a threshold applied to the resulting image. The threshold was chosen to be just below the first photon peak, determined from examining a histogram of the data with the background subtracted. The oversampling ratio [38], σ, (which is defined for a dimension to be the number of pixels in the object divided by the total number of pixels) after binning was $\sigma_x = 8.3$ and $\sigma_y = 15.2$ for x and y respectively. This degree of oversampling is large enough that it has negligible effect [39] on the diffraction pattern due to the finite width of the detector pixels. Shown in Supplementary Figure S1 are comparisons of the reconstructed intensity with the measured data for both the full coherence and the partially coherent reconstruction methods. Three intensities are shown for comparison with the measured intensity, I^m. The intensities are as follows; $I^a = |\psi_c^k|^2$ is the estimate of the measured intensity assuming full coherence, $I^u = I^v \otimes \gamma^k$, is the estimate for the measured intensity from the partially coherent method outlined in the main text, and $I^v = |\psi_{pc}^k|^2$ is the estimate of the coherent intensity from the partially coherent method. A quantitative comparison can be made between the reconstructed intensities with those measured. Shown in Supplementary Figure S2 is a plot of the error metric, χ^2 defined by,

$$\chi^2 = \frac{\sum_{j=1}^{J} |\sqrt{I^m(j)} - \sqrt{I_x^k(j)}|^2}{\sum_{j=1}^{J} I^m(j)}, \tag{S1}$$

where j is the pixel, J is the total number of pixels, I^m is the measured data and I_x^k is the estimate of the measured data during the iterative procedure. The error metric corresponds to the reconstruction shown in the main text using the 'low' coherence data. The subscript x denotes whether the comparison is made assuming full coherence, $x = c$ (red line), or during the partially coherent reconstruction, $x = pc$ (blue line), with $I_c^k = |\psi_c^k|^2$ and $I_{pc}^k = |\psi_{pc}^k|^2 \otimes \gamma^k$. The final χ^2 for the partially coherent reconstruction ($\chi^2 = 2.1 \times 10^{-2}$) is lower than the reconstruction assuming full coherence ($\chi^2 = 2.4 \times 10^{-2}$) indicating better agreement with the measured data. The periodicity of the support constraint is evident (updated every 5 iterations) in the error, as well as the update for γ^k (every 15 iterations) during the partially coherent reconstruction (blue line). The parameter choice for the reconstruction algorithm were not critical to its success and were mostly conservative. Choices of algorithm and support constraint parameters vary between many examples of CDI. As has been stated previously [40,41], no deterministic algorithm exists for iterative phase retrieval. As a consequence many combinations of parameters exist in the literature. The most critical choice of parameters relate to the choice for support, but this is reliably solved by the shrinkwrap[35] method. The choice of parameters for the updating of the numerical estimate for the Mutual Coherence Function (MCF) were chosen largely based on reducing computation time. It was found that updating the MCF every iteration led to slower convergence. The process is also sped up by using the previous output as the input for the next update.

To compare the reconstructed normalised MCF to what is expected, we need to estimate the coherence properties in the horizontal direction. Assuming a Gaussian source, the transverse coherence length (taken as the half-width at half maximum of $|\gamma|$) for a given transverse direction is[24]

$l_T = (2\lambda L)/(\pi D)\sqrt{(}\ln(2))$ where L is the distance from the source and D is a characteristic source size. Source defining slits 20 m before the roller blade slits were set at $D = \sigma_x = 150$ μm at a wavelength of 1.39 Å giving $l_x \simeq 10$ μm. If we assume the source to be described by the Gaussian-Schell model, then the ratio of the beam size to the coherence length for a particular direction will remain constant[25]. Typical focussed beam sizes are 1.0-1.5 μm (measured by fitting an error function to a knife edge scan) which gives an approximate coherence length at the sample position of between 200-300 nm for a roller blade slit setting of 50 μm. The recovered half-width at half maximum of $|\gamma|$ for x and z are 220 and 485 nm respectively. The longitudinal coherence properties have previously been measured and were found to be Gaussian with a half-width at half maximum of 660 nm [12]. The two recovered coherence lengths obtained here of 220 and 485 nm for x and z respectively are in good agreement with estimated and previously measured coherence lengths for x and z of 200-300 nm and 660 nm.

For the case of a dynamic $\gamma(\boldsymbol{x})$, as could be found from recording many shots from an identical sample with an XFEL source, we can write the accumulated intensity $\langle I_{\text{pc}}(\boldsymbol{q})\rangle\rangle$ as an incoherent sum of each shot via,

$$\langle I_{\text{pc}}(\boldsymbol{q})\rangle = \sum_{i}^{N} I_i(\boldsymbol{q}), \tag{S2}$$

where i is shot number and N is the total number of shots. Each intensity is given by,

$$I_i(\boldsymbol{q}) = I_c(\boldsymbol{q}) \otimes \hat{\gamma}_i(\boldsymbol{q}), \tag{S3}$$

where $I_c(\boldsymbol{q})$ is the coherently diffracted intensity from the sample and $\hat{\gamma}_i(\boldsymbol{q})$ is the far-field representation of the normalised MCF for shot i. Inserting equation S3 into equation S2 we get,

$$\langle I_{\text{pc}}(\boldsymbol{q})\rangle = \sum_i^N I_c(\boldsymbol{q}) \otimes \hat{\gamma}_i(\boldsymbol{q}) \tag{S4}$$

$$= I_c(\boldsymbol{q}) \otimes \hat{\gamma}_1(\boldsymbol{q}) + I_c(\boldsymbol{q}) \otimes \hat{\gamma}_2(\boldsymbol{q}) + \cdots + I_c(\boldsymbol{q}) \otimes \hat{\gamma}_N(\boldsymbol{q}) \tag{S5}$$

$$= (N) I_c(\boldsymbol{q}) \otimes \sum_i^N \hat{\gamma}_i(\boldsymbol{q}) \tag{S6}$$

$$= (N) I_c(\boldsymbol{q}) \otimes \langle \hat{\gamma}(\boldsymbol{q})\rangle \tag{S7}$$

where $\langle \hat{\gamma}(\boldsymbol{q})\rangle$ is the 'average' coherence properties with its definition implied by equation S6. Equation S7 is precisely the from that is amenable to the method described here, where $\langle \hat{\gamma}(\boldsymbol{q})\rangle$ is the 'average' of the MCF at the detector.

The coordinates used to measure the data are CCD detector pixels (x and y) and the deviation from the Bragg angle θ. This non-orthogonal three-dimensional grid in reciprocal space transforms into a non-orthogonal real space grid containing the images [42]. We use a coordinate transformation to convert this to a Cartesian laboratory frame. The measured reciprocal space coordinates are denoted as $\boldsymbol{q} := (\boldsymbol{q}_1, \boldsymbol{q}_2, \boldsymbol{q}_3)$ with $\boldsymbol{q}_1$ and $\boldsymbol{q}_2$ running transverse to the detector face and $\boldsymbol{q}_3$ being the scan direction. The real space coordinates resulting from the measurement are denoted as $\boldsymbol{r} := (\boldsymbol{r_1}, \boldsymbol{r_2}, \boldsymbol{r_3})$ which in general will not be the same as the laboratory reference frame $\boldsymbol{x}$, $\boldsymbol{y}$ and $\boldsymbol{z}$, with $\boldsymbol{x}$ and $\boldsymbol{y}$ are transverse to the beam direction and $\boldsymbol{z}$ is parallel. The relationship between a point $\boldsymbol{P}$ in the orthogonal laboratory frame and a point $\boldsymbol{P}'$ in the reconstructed frame is $\boldsymbol{P} = \boldsymbol{P}'\boldsymbol{T}$ where $\boldsymbol{T}$ is the transformation matrix. For the setup at beamline 34 at the Advanced Photon Source

$\boldsymbol{T}$ is given by

$$\boldsymbol{T} = \epsilon \begin{pmatrix} -\alpha \sin(\delta)\cos^2(\gamma) & 0 & \kappa \cos^2(\gamma)\sin(\delta) \\ \alpha \cos(\delta)\sin(\gamma) - \alpha \sin(\gamma)\cos(\gamma) & -\beta \cos(\gamma)\sin(\delta) & \kappa \cos(\gamma)\sin(\gamma) \\ \alpha \cos(\gamma) - \alpha \cos^2(\gamma)\cos(\delta) & 0 & \kappa \cos^2(\gamma)\cos(\delta) \end{pmatrix}, \quad \text{(S8)}$$

where δ is the angle made between the detector arm and the beam direction in the horizontal $z-x$ laboratory plane, γ is the angle made by the detector arm from the horizontal in the $z-y$ plane, $\epsilon = (\sin(\delta)\cos^2(\gamma))^{-1}$, $\alpha = (N_x \Delta x)/(d\lambda)$, $\beta = (N_y \Delta y)/(d\lambda)$, $\kappa = (N_s \Delta\theta)/(\lambda)$, $\Delta x, \Delta y$ are the detector pixel sizes, $\Delta\theta$ is the scan step size, N_x, N_y and N_s are the number of pixels in the horizontal, vertical and scan directions respectively, d is the sample to detector distance and λ is the wavelength. While these transformations are specific to the 34-ID-C instrument, they should apply widely to all experiments performed there and are relatively easy to modify for other installations of CDI.

Supplementary References

38. Miao, J., Sayre, D. & Chapman, H. N. Phase retrieval from the magnitude of the fourier transforms of nonperiodic objects. *J. Opt. Soc. Am. A* **15**, 1662 (1998).

39. Song, C. *et al.* Phase retrieval from exactly oversampled diffraction intensity through deconvolution. *Phys. Rev. B* **75**, 012102 (2007).

40. Elser, V. Phase retrieval by iterated projections. *J. Opt. Soc. Am. A* **20**, 40–55 (2003).

41. Quiney, H. Coherent diffractive imaging using short wavelength light sources. *Journal of Modern Optics* **57**, 1109–1149 (2010).

42. Pfeifer, M. A. *Structural Studies of Lead Nanocrystals using Coherent X-ray Diffraction.* Ph.D. thesis, University of Illinois (2004).